Supporting Information

Donahue et al. 10.1073/pnas.1115186109

SI Text

2D Volatility Basis Set Modeling. The kinetic model employed in this work employs a 2D volatility basis set similar to those described in Jimenez et al. (1), Donahue et al., (2) and Murphy et al., (3). The model describes the evolution in volatility and oxygenation in the context of a thermodynamic framework described in Donahue et al., (4). The "basis set" refers to discretization of this 2D space to form lumped organic species characterized by their volatility and extent of oxidation. The key parameters in the 2D-VBS are volatility (C^*), given as a saturation mass concentration in $\mu g\,m^{-3}$ (essentially the saturation vapor pressure in mass units) and oxygenation, given as either O:C or the mean oxidation state of carbon, $\overline{OS}_C$. The thermodynamic framework gives the average molecular composition (carbon, hydrogen and oxygen numbers, n_C, n_H, and n_O) as functions of C^* and O:C, also based on an observationally constrained relationship between O:C and $\overline{OS}_C$ (4).

The equilibrium phase partitioning of this mixture is driven by the total mass concentration of organic aerosol (C_{OA}) distributed over decadally spaced volatility "bins" described by C_i^* at 298 K. The mass fraction ξ_i in the condensed phase in each bin i with volatility C_i^* and C_{OA} are given recursively by

$$\xi_i = (1 + C_i^*/C_{OA})^{-1}; \qquad C_{OA} = \sum_i \xi_i C_i, \qquad \textbf{[S1]}$$

where $C_i = C_i^v + C_i^a$ is the total (vapor- plus aerosol-phase) concentration of i, as described by Donahue et al., (5). For the model described here, we assume that the particles reach their equilibrium state within roughly 10,000s, which is the rough timescale for oxidation. This equilibrium timescale is equivalent to assuming that the mean diffusivity of organics in the particles is $\geq 10^{-14}\ cm^2\,s^{-1}$. We also assume ideal solution behavior, meaning that $C_i^* = C_i^o$, the pure sub-cooled liquid saturation mass concentration of i. The subcooled liquid value is appropriate even if the aerosol is in a glassy state because it provides the best estimate of the enthalpy and entropy of vaporization for an amorphous condensed phase.

The partitioning in Eq. **S1** is for a 1D volatility basis set. In the ideal 2D case with dimension i representing volatility and dimension j representing oxidation, we use the shorthand $C_i = \sum_j C_{i,j}$ to represent the sum over all oxidation states at a given volatility. Eq. **S1** can be solved directly in the 2D-VBS for *all* volatility bins, though one must be careful with the numerics because decimally separated bins are relatively well conditioned, while (in the non-ideal case) more closely spaced bins can generate a stiffer iteration (even without considering liquid-liquid phase separation).

The issues for the chemical mechanism described here are how compounds at a given C^*, O:C location (bin i, j) evolve after reaction with OH radicals and how these species in either the gas or condensed phase interact with the chamber walls. For the simulations described in this work, we assume that all organic vapors react with OH with a common rate constant of $k_{i,j}^v = 3 \times 10^{-11}\ cm^3\,molec^{-1}\,s^{-1}$. Heterogeneous uptake of OH to particles can also oxidize organic material. In this box model we do not resolve the aerosol size distribution, so instead of directly calculating OH uptake based on a condensational sink and an (uncertain) OH uptake coefficient, we parameterize OH uptake with an effective OH rate constant that is slower than the gas-phase rate constant by an adjustable retardation factor. This factor is based on microphysical calculations for typical 200–400 nm particles; our best estimate is that heterogeneous uptake is roughly a factor of 10 slower than homogeneous oxidation if OH uptake is uninhibited ($\alpha = 1$), so $k_{i,j}^a = k_{i,j}^v/10$. Consequently, we present model calculations for a retardation factor of 5 as an upper limit for the effect of heterogenous oxidation and a factor of ∞ as a lower limit. Those limits are indicated by the solid (lower limit) and dashed (upper limit) curves in Fig. 1*B*. The effect is modest in the early phase of OH aging because gas-phase oxidation is rapid and continued production of low C^* products by that gas-phase oxidation is also substantial. However, as the system becomes aged and semivolatile organic vapors are depleted, the heterogeneous uptake becomes more significant. After the equivalent of about 1 d (12 daylight hours) under typical conditions (2.5 h with the elevated OH in Fig. 1*B*, heterogeneous oxidation and consequent loss of OA mass via fragmentation is the dominant process in the simulation. We do not believe that the Multiple Chamber Aerosol Chemical Aging Study (MUCHACHAS) experiments provide a significant constraint regarding heterogeneous uptake, but the simulations suggest that it could be of major importance during long-range transport of OA in the remote atmosphere.

For use in a box model, we discretize the space to form a VBS with $C_{i,j}^*$ ranging (i) from 10^{-5} to $10^9\ \mu g\,m^{-3}$, separated by powers of 10, and O:C ranging (j) from 0 to 1, separated by 0.1. The bins with $C^* \geq 10^6\ \mu g\,m^{-3}$ (the VOCs) are included only for completeness and to conserve mass; any operational model would explicitly model the VOCs and oxygenated VOCs (OVOCs) in that range (as indeed we explicitly model the precursor α-pinene loss). To simulate the chemistry of vapors in the 2D-VBS, we have constructed two "oxidation kernels" representing two competing processes, functionalization and fragmentation, as described in Jimenez et al. (1) and the supplemental material of that work. In the 2D-VBS framework we track carbon mass and compute the total organic mass to ensure mass conservation, and compute the total mass concentration in each bin explicitly given the OM:OC ratio and the known average carbon, hydrogen and oxygen numbers (n_C, n_H, n_O) in each bin.

The lumped mechanism consists of a large ensemble of transformation matrices, each of which represents the product distribution of compounds. The matrices describe the (carbon mass) transformation from a source bin (i, j) to a distribution of product bins (k, l). Examples of functionalization ($F_{i,j;k,l}$) and fragmentation ($R_{i,j;k,l}$) matrices are shown in Fig. S1*A* and *B*. For the model employed here there are 165 such matrices for each kernel, or 330 in total. Note that, mathematically, the full transformation from source bins i, k to product bins k, l is really a single 165×165 transformation matrix, but visualization of that matrix is impossible. Once the full transformation matrices are developed based on the constraints described below, the governing differential equation for the 2D-VBS mechanism can be written:

$$\begin{aligned}\frac{dC_{i,j}}{dt} = &+\sum_{k,l}[(1-\beta_{k,l})F_{i,j;k,l} + \beta_{k,l}R_{i,j;k,l}]k_{k,l}^v C_{k,l}^v C_{OH} \\ &+\sum_{k,l}[(1-\beta_{k,l})F_{i,j;k,l} + \beta_{k,l}R_{i,j;k,l}]k_{k,l}^a C_{k,l}^a C_{OH} \\ &-(k_{i,j}^v C_{i,j}^v + k_{i,j}^a C_{i,j}^a)C_{OH}. \qquad \textbf{[S2]}\end{aligned}$$

Eq. **S2** is solved numerically and (equilibrium) partitioning is calculated at each step, governed by Eq. **S1**, to give the various model simulation figures.

Functionalization is formation of a product with an identical carbon number to a precursor but increased O:C, while fragmen-

tation is formation of at least two products with lower carbon numbers (as well as an increased O:C for the aggregate). The two kernels are designed to incorporate best estimates for the aggregate change in volatility and oxygenation over one step of oxidation from a stable molecular reactant to a distribution of stable molecular products. Organic radical intermediates are not treated explicitly, though we can simulate the effect of RO_2 branching by generating kernels for high NO_x (dominated by $RO_2 + NO$) and low-NO_x (dominated by $RO_2 + HO_2$) and blending those product distributions based on RO_2 branching predicted by the chemical mechanism depicting VOC chemistry. For the simulations described here we used one kernel for functionalization and one for fragmentation, neglecting any NO_x dependency to the chemistry.

For the functionalization kernel we assume that each generation of oxidation by OH that does not cause fragmentation reduces C^* by between one and six decades (mostly 2–4 decades) and adds between one and three oxygen atoms (with the change in O:C depending on the mean carbon number of a given starting bin). The foundation for this assumption is the group contribution method underlying the 2D volatility framework (4) coupled with a standard model that OH oxidation typically adds about one (−OH) group (dropping C^* by about 2.5 decades) and one (=O) (dropping C^* by about 1 decade). A key simplifying assumption is that reactions in the functionalization branch will be similar for all bins in the 2D-VBS. The functionalization behavior is represented by a functionalization kernel describing that evolution in C^* and carbon number.

A sample functionalization matrix for chemistry out of the bin at $C^* = 10\ \mu g\,m^{-3}$, O:C = 0.5 is shown in Fig. S1*A*. We assume that oxidation reactions add on average two oxygen atoms, 1 (−OH) and 1 (=O), and consequently decrease C^* by about 3.5 decades (this is also consistent with organic acid functionalization, which is a specialized form of the nominal hydroxy carbonyl functionalization. Thus in Fig. S1*A* the most likely outcome of a functionalization reaction is a decrease of three decades in C^*, but there is a high probability of a four decade decrease. In addition to the typical functionalization, some products contain more (−OH) functionalization and some contain more (=O) functionalization, while some products contain three oxygen functionalities and some only one. This kernel is used to develop a succession of normalized functionalization matrices describing the product distribution (carbon mass yields) for productions from each bin in the 2D-VBS (normalized in this case means that the sum of all carbon mass yields is 1. Distributing the products in the x direction (C^*) is straightforward, while the y-direction (O:C) depends on the average carbon number of the starting bin (and thus the products), which is known. In simple terms, the kernel aligns along lines of constant carbon number shown in Donahue et al. (4), as the carbon number is assumed to be constant, but it is not a perfect diagonal because we assume that the chemistry *on average* adds one (−OH) functional group for every (=O) functional group, but there is a distribution around this average represented by the kernel, and that influences volatility. Without question there is uncertainty in this functionalization kernel, but the average behavior of one generation of OH oxidation chemistry is fairly well constrained in the absence of fragmentation.

For fragmentation, we assume that the mixture of molecules in a given bin is rich. Especially because fragmentation becomes important with increasing O:C, the varied precursors will have led to an even more complex mixture of products, so the compounds in a given bin (representing the *precursors* for the oxidation step in question) will have functional groups in many locations along the carbon backbone. Consequently, we assume that the cleaving C−C bond is randomly distributed along the carbon backbone, resulting in an even *molar* distribution for all carbon numbers between C_{n-1} and C_1. Indeed the C_{n-1} and C_1 molar yields *must* be the same to conserve carbon, as must the C_{n-2} and C_2 molar yields, etc. The even molar distribution means that the carbon *mass* in the products is a triangular distribution weighted toward the heavy products. We assume that this triangular distribution applies to all C^* bins more volatile than a given precursor (this is one reason we extend the volatilities up through the VOC range). For example, if a precursor with $C^* = 1\ \mu g\,m^{-3}$ fragments, the $C^* = 10\ \mu g\,m^{-3}$ bin will receive the most carbon mass, and the $C^* = 10^9\ \mu g\,m^{-3}$ bin the least, with a normalized distribution. Normalized in this context means that the total carbon mass is conserved, and also that the sum of the masses for paired bins in the product distribution are all the same. Thus if the carbon mass is spread over 10 different volatility bins, the sum of the carbon mass S in bin 10 and bin 1 will be equal to the sum in 9 and 2, etc. However, bin 10 will contain $0.91S$ while bin 1 will contain $0.09S$, bin 9 will contain $0.82S$ while bin 2 will contain $0.18S$, etc.

We also need to assign an O:C to these products. The simplest thing to do would be to assign all of the products the same O:C as the precursor, in which case fragmentation would be exclusively a horizontal move toward higher volatility. However, because the smallest fragments are often highly oxidized (CO, CH_2O, etc), we assume that the less-volatile bins to the left of the midpoint (nominally $C_{n/2}$) have the same O:C as the precursor, while the more volatile bins to the right of the midpoint (more volatile) progress diagonally with progressively rising O:C toward the bin with the highest O:C (i.e., $C^* = 10^9\ \mu g\,m^{-3}$, O:C = 1.0).

An added complication in the fragmentation step is that reacting molecules almost never decompose into two stable molecules. Consequently, the process described above represents the first in a two-step process connecting a precursor molecule (bin) to a succession of product molecules (bins). The "product" bins just described are really seeds for a further functionalization step, which distributes the final stable products of the fragmentation process toward lower volatility and higher O:C. The initial fragments are assumed to be evenly split between a molecular and a radical fragment, meaning that half of the products remain in the product bins just described, while half are functionalized. This kernel is similar to the one shown above, with the major difference being that many heavy fragments are assumed to end up with roughly the same C^* and O:C as the seed because they are in fact stable molecules. Fragmentation thus fills the wide area in the 2D space, as shown in Fig. S1*B*. While we regard the functionalization kernel as being relatively well constrained by a priori considerations, the fragmentation kernel is far less well constrained. The basics are clear—fragmentation often occurs when there is one stable molecular decomposition product and one radical product—but the rest, including the assumption of an equal probability of cleavage among all C−C bonds, on average, is more speculative.

In addition to defining the two kernels, we must define the branching ratio (β) between them. Fragmentation in this 2D model becomes progressively more important as molecules become more oxidized. The motivation is that functionalization about C−C bonds generally weakens them and promotes decomposition—this is supported by an enormous body of research into hydrocarbon oxidation. We have adopted a functional form for β using a simple function of O:C—specifically $\beta = (O{:}C)^n$. For the results shown here we have assumed $\beta = (O{:}C)^{(1/4)}$, whereas previously we have used $\beta = (O{:}C)^{(1/6)}$. This exponent means that compounds with an O:C of 0.5 have a 84% chance of fragmenting [with $n = (1/6)$ it was 90%]. Fragmentation rises sharply for O:C < 0.5 and is almost complete above that value. This is truly a parameterization. There is no fundamental basis for the assumed functional form; the form simply has some salubrious characteristics with a rapid rise in fragmentation at low O:C followed by a smooth approach to 100% fragmentation for the largest O:C in the model (1:1).

In Fig. S2 we show the sensitivity of the model calculation to different values of this parameter for atmospherically relevant

organic-aerosol levels, with high OH of 10^7 molec cm^{-3} as in Fig. 1*B*. The value used in earlier publications ($O:C^{1/6}$) gives a factor of 3 enhancement while the value used here ($O:C^{1/4}$) gives a factor of 4 enhancement in the SOA levels. While this quantitative difference is important, it in no way influences any of the major conclusions of this work. For this simulation we have also set the effective heterogeneous oxidation rate constant a factor of 10 slower than the homogeneous gas-phase rate constant, which is the geometric mean of the two values used in Fig. 1*B* (5 × slower and infinitely slower). The middle, solid green curve here thus represents our best estimate of the likely effect of OH aging on a plume of SOA over the course of roughly 1 w under normal atmospheric conditions.

Wall losses and dilution. The box model must address physical losses as well, as the models simulate the suspended aerosol and gas-phase mass concentrations. There are three major loss processes: Dilution, vapor deposition to walls, and particle deposition to walls. For the model, each is treated with a first-order rate constant that is independent of the x and y values in the 2D VBS mechanism (all material in any given phase is treated identically). Treating all compounds identically is obviously an oversimplification, and it would be trivial but meaningless to "tune up" the model by adjusting the parameters if we freed them up.

For the model runs described in this paper, we track four categories of material (in addition to the precursor) in the 2D-VBS as a mass concentration of carbon (Figs. S3–S5): Suspended vapors, suspended particles, wall-bound particles, and lost mass (for dilution and irreversible wall losses, tracked only to ensure carbon balance).

One complication is that, in all but the HOOH photolysis experiments, OH radicals were also produced during the α-pinene ozonolysis, with a molar yield between 0.8 and 1.0 (6). Most of these OH radicals certainly reacted with α-pinene (the OH + α-pinene rate constant is gas-kinetic (6) and 3–10 times faster than reactions with first-generation products), but a small fraction reacted with first-generation products as well. While OH reactions with α-pinene lead to a somewhat different product distribution than pure ozonolysis as well as slightly higher overall SOA mass yields (7), the chemistry still ended with complete consumption of the α-pinene; consequently, the essential MUCHACHAS design was not affected. HOOH is unique because, in the dark, it acts as an OH-radical scavenger, converting OH to HO_2, but with UV lights on it is an OH-radical source. As a scavenger, HOOH also leads to higher SOA yields than other scavengers, similar to unscavenged experiments (8); consequently we have used a single product distribution for SOA formation from α-pinene, with a stoichiometry of 1.8 moles of product per mole of ozone + α-pinene reacted to account for additional pinene consumption by OH. This product distribution is shown in Fig. 1*A*.

Dilution is the simplest loss to treat—a dilution rate constant causes first-order loss of both vapors and suspended particles to the "waste" bins. During MUCHACHAS, only the SAPHIR experiments had substantial dilution.

Particle deposition to the walls is treated as a first-order process converting suspended particle mass into wall-bound particle mass. This treatment incorporates an assumption that SOA particles do not wet (or react with) the chamber walls and thus remain physically intact after adhering to the walls. Wall deposition is important to the overall mass balance because the particles will continue to communicate with the organic vapors. As a consequence of this assumption, the composition of the wall-bound and suspended particles must be the same at true equilibrium (composition in this consequence means the mixing ratios of all modeled 2D-VBS constituents in the particles) as long as the particles are large enough for the Kelvin (curvature) term to be negligible (which they are).

Wall deposition and the subsequent behavior of deposited material constitutes a major uncertainty, as the wall-bound particles are not observed; however, a strength of MUCHACHAS is the very different behaviors of the chambers. The SAPHIR, PSI, and CMU chambers are all teflon, but the relative timescales for chemical transformation and wall deposition are very different. An example is shown in Fig. S3 for the PSI chamber. At the onset of aging ($t = 0$), slightly more than half of the SOA mass exists as wall-bound particles. In the model, the wall-bound and suspended particles are assumed to remain in equilibrium, meaning that when chemistry produces condensible vapors, the fraction of those vapors that condenses on suspended particles is equal to the fraction of the particle mass that is suspended. At $t = 0$ in the experiment shown in Fig. S3 about 40% of the condensible vapors produced via OH aging condense on the suspended particles, but as the simulation continues that fraction becomes very small (and consequently the observed mass growth becomes correspondingly small).

In contrast, conditions in the AIDA chamber are modeled with very different assumptions. In AIDA particle deposition to the walls is very slow, but reactive organic vapors are lost irreversibly to the aluminum walls. In the model this loss is treated with a single vapor deposition time constant based on earlier experiments (9). Consequently, whereas the model for the PSI experiment shown in Fig. S3 contains a substantial pool of vapors (the dotted blue curve), the model for the AIDA experiment shown in Fig. S4 is very depleted in vapors. This vapor depletion is a conservative assumption as actual deposition is strongest for organic acids, which tend to be at the low end of the C^* distribution; for example during MUCHACHAS experiments, cis-pinonic acid was lost to the walls very rapidly while pinonaldehyde was stable (before reacting with OH). The model, however, produces vapors that condense reversibly only to suspended particles, while they are also lost to the aluminum walls (from the vapor phase only).

The mass losses of the suspended particles shown in Fig. S4 (in the solid green curve for the model and the green circles for the observations) are associated with mass losses from the suspended particles, which shrank to a degree quantitatively consistent with the observed mass loss. This mass loss confirms that the particles were semivolatile. It vapor mass loss also explains the change in the loss rate evident in Fig. S4 before and after aging. Before aging the model SOA consists almost entirely of semivolatile species, which are lost to the walls in proportion to their mass fraction in the gas phase. After aging a significant fraction of the modeled SOA mass is transformed to less volatile species, which have a lower gas-phase mass fraction and thus a longer lifetime in AIDA. An example is the conversion of cis-pinonic acid (more than 90% in the gas phase, as seen in Fig. 1*A*) to MBTCA (99.99% condensed). The vapors deposited to the walls are shown in Fig. S4 as a dotted magenta curve. This deposition is assumed to be irreversible and consequently they do not participate in subsequent phase partitioning in any way.

While condensation to the walls is clearly a major uncertainty, the relatively good performance of the model under very different conditions, shown in Fig. 2 and Figs. S3–S5, strongly supports our overall conclusions that gas-phase aging of first-generation SOA vapors is a major contributor to OA behavior on atmospheric timescales of hours to days. The particle behaviors were consistent with our model assumptions. In teflon chambers, SOA particles remained at a constant diameter after formation, until they grew during aging chemistry. That stability is consistent with reversible wall interactions and a stable pool of gas-phase semivolatile organics. In the aluminum AIDA chamber, particles shrank after formation. That shrinking is consistent with losses of semivolatile organic vapors. The assumed condensation of vapors to particles bound to the wall, as in Fig. S3, is highly uncertain but this assumption is completely different from the deposition assumed in the AIDA chamber. The congruence of the model

results for these two qualitatively different situations greatly strengthens our conclusions.

While we could attempt to formulate a "best guess" set of parameters, we instead restricted ourselves to only two model adjustments: We slightly adjusted (by <10%) the initial α-pinene levels so that the SOA mass concentration at $t = 0$ matched the observations, and we changed the fragmentation exponent from our initial guess of 1/6 to 1/4 as discussed above. By keeping the model "clean" we have done our best to present a fair comparison of the hypothesized effects of gas-phase aging chemistry and the resulting MUCHACHAS observations.

A final encouraging result, mentioned in the main text, is the coincidence between the PSI and CMU results using HONO photolysis as the OH source. The CMU HONO photolysis data are shown in Fig. S5.

1. Jimenez JL, et al. (2009) Evolution of organic aerosols in the atmosphere: A new framework connecting measurements to models. *Science* 326:1525–1529.
2. Donahue NM, Kroll JH, Robinson AL, Pandis SN (2012) A 2D volatility basis set: 2. Diagnostics of laboratory and ambient organic aerosol. *Atmos Chem Phys*. 12:615–634.
3. Murphy BN, Donahue NM, Pandis SN (2011) Simulating the oxygen content of ambient organic aerosol with the 2D volatility basis set. *Atmos Chem Phys* 11:7859–7873.
4. Donahue NM, Epstein SA, Pandis SN, Robinson AL (2011) A 2-dimensional volatility basis set: 1. Organic mixing thermodynamics. *Atmos Chem Phys* 11:3303–3318.
5. Donahue NM, Robinson AL, Stanier CO, Pandis SN (2006) Coupled partitioning, dilution, and chemical aging of semivolatile organics. *Environ Sci Technol* 40:2635–2643.
6. Calvert J, et al. (2000) *The Mechanisms of Atmospheric Oxidation of the Alkenes* (Oxford University Press, New York).
7. Iinuma Y, et al. (2005) Laboratory studies on secondary organic aerosol formation from terpenes. *Faraday Discuss* 130:279–294.
8. Henry KM, Donahue NM (2011) Effect of the OH radical scavenger hydrogen peroxide on secondary organic aerosol formation from α-pinene ozonolysis. *Aerosol Sci Technol* 45:686–690.
9. Saathoff H, et al. (2009) Temperature dependence of yields of secondary organic aerosols from the ozonolysis of α-pinene and limonene. *Atmos Chem Phys* 9:1551–1577.

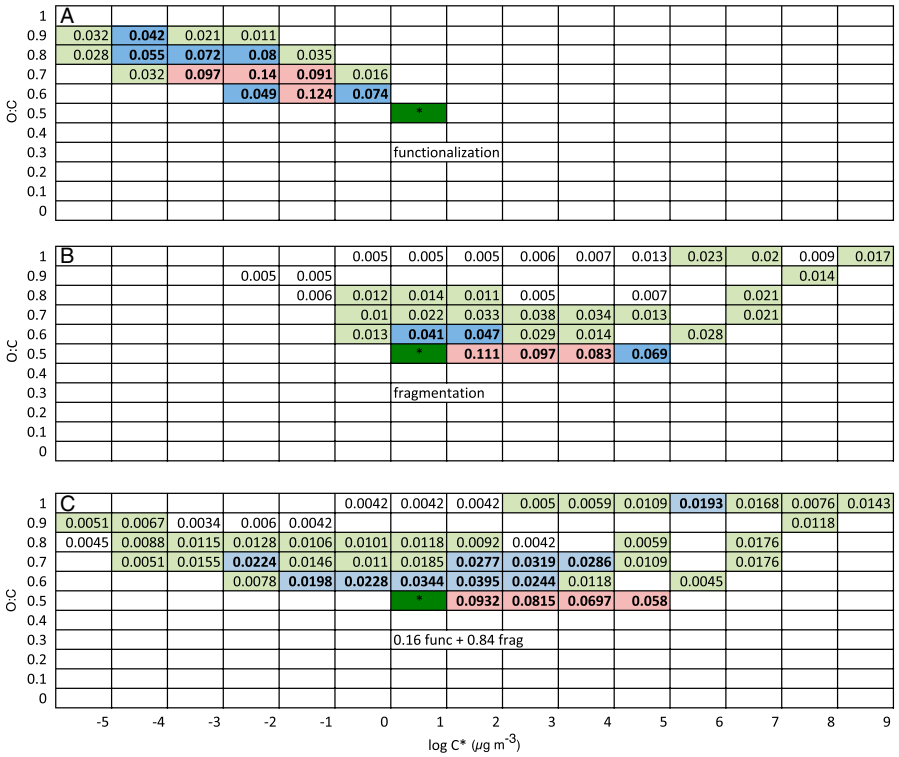

Fig. S1. Example oxidation matrices for functionalization, $F_{i,j;k,l}$ (a, top), fragmentation, $R_{i,j;k,l}$ (b, middle) and the weighted sum of these two, $[(1-\beta_{k,l})F_{i,j;k,l} + \beta_{k,l}R_{i,j;k,l}]$ (c, bottom) for OH oxidation of material in the $C^* = 10$ μg m^{-3}, O:C = 0.5 bin (i, j) of the discretized 2D VBS (indicated by the green shaded box with an asterisk (*). The matrices show the fractional carbon yield in each bin from the green-shaded source bin for one generation of OH oxidation. For a fragmentation branching ratio $\beta = \text{O:C}^{(1/4)}$ these products have an 84% chance of fragmentation, so the weighting for the lower box is $0.16F + 0.84R$. For *A* and *B*, product bins with yields >0.08 are shaded red, those with yields >0.04 are shaded blue, and those with yields >0.01 are shaded olive. In *C* these thresholds are 0.04, 0.02, and 0.005. Because some of the fragmentation products have a lower C^* than the precursor, the overall yield of products less volatile than the precursor is 0.21, while the yield of products more volatile than the precursor is 0.63. The remainder (0.16) move up in O:C with no change in volatility, as the effects of fragmentation are offset by additional oxygenated functional groups.

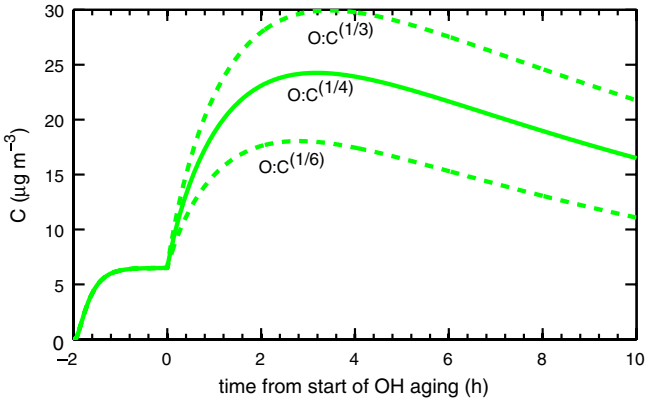

Fig. S2. Consequences of different fragmentation parameterizations. Simulations are for low initial α-pinene (50 μg m^{-3}) as in the lower-mass curves of Fig. 1*B*. Here we have assumed the best-estimate value for heterogeneous uptake a factor of 10 slower than homogeneous gas-phase OH oxidation and three values of the fragmentation exponent $\beta = O{:}C^{n}$; $n = 1/3$, 1/4; 1/6. While the quantitative enhancement of SOA levels due to aging changes with fragmentation, and the timing of the maximum changes slightly, the essential feature of substantial mass enhancement by a factor of 3–5 does not change.

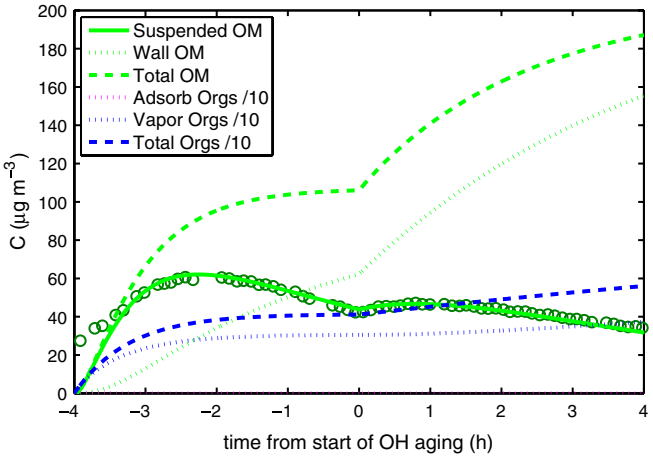

Fig. S3. Complete model results for a MUCHACHAS experiment in the PSI chamber (with higher total SOA mass than the experiment in Fig. 2*C*). Different reservoirs are indicated with different curves, as shown in the legend. Total Orgs includes all carbonaceous oxidation products (including CO and CO_2) but not the precursor α-pinene, which is lost over the first 2 h (causing the rise in Total Orgs). The vapor concentrations (in blue) are divided by 10 to keep them on scale.

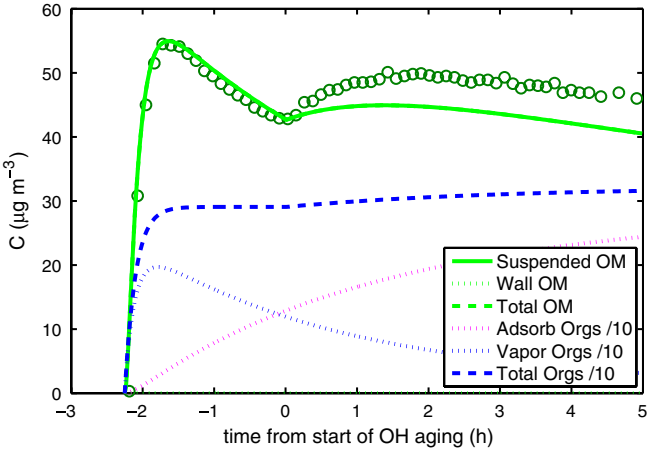

Fig. S4. Complete model results for a MUCHACHAS experiment in the AIDA chamber. Different reservoirs are indicated with different curves, as shown in the legend. Organic vapors are lost irreversibly to the aluminum chamber walls, shown with the magenta dotted curve marked "Adsorb Orgs". Adsorbed organics rapidly becomes the dominant carbon reservoir.

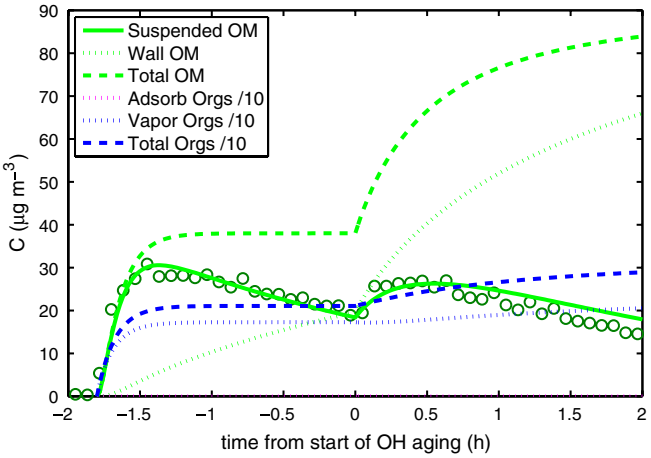

Fig. S5. HONO photolysis aging experiment in the CMU chamber. Results are very similar to the rapid OH aging at the PSI chamber shown in Fig. S3 and Fig. 2*A* of the main text.

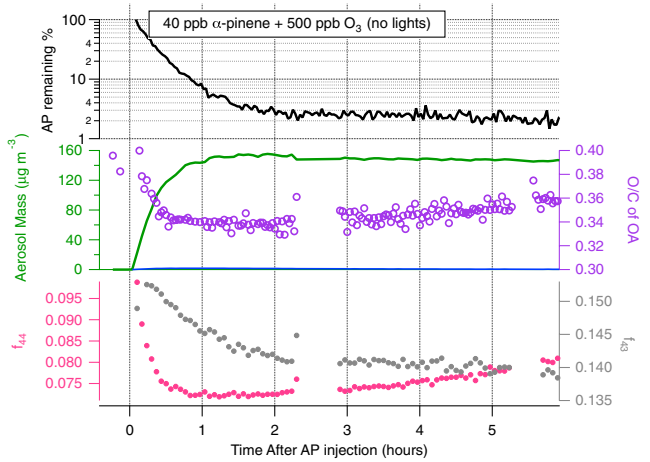

Fig. S6. Time trace of a "ripening" experiment at PSI without OH-driven aging. Once 90% of the α-pinene (AP, black) is consumed after 1 h, the total aerosol mass (green) is stable but key peaks in the mass spectrum evolve. The fraction of the signal at m/z = 43 (gray) steadily decreases, while the fraction at m/z = 44 (pink) steadily increases. The calculated total O:C (violet) is nearly constant between hours 1 and 4 and drifts slightly upward afterwards.